Soft-matter capacitors and inductors for hyperelastic strain sensing and stretchable electronics

2013 Smart Mater. Struct. 22 055023

(http://iopscience.iop.org/0964-1726/22/5/055023)

IOP Publishing Smart Materials and Structures
Smart Mater. Struct. **22** (2013) 055023 (8pp) doi:10.1088/0964-1726/22/5/055023

Soft-matter capacitors and inductors for hyperelastic strain sensing and stretchable electronics

A Fassler and C Majidi

Department of Mechanical Engineering, Carnegie Mellon University, Pittsburgh, PA 15213, USA

E-mail: afassler@andrew.cmu.edu

Received 14 October 2012, in final form 18 January 2013
Published 11 April 2013
Online at stacks.iop.org/SMS/22/055023

Abstract
We introduce a family of soft-matter capacitors and inductors composed of microchannels of liquid-phase gallium–indium–tin alloy (galinstan) embedded in a soft silicone elastomer (Ecoflex® 00-30). In contrast to conventional (rigid) electronics, these circuit elements remain electronically functional even when stretched to several times their natural length. As the surrounding elastomer stretches, the capacitance and inductance of the embedded liquid channels change monotonically. Using a custom-built loading apparatus, we experimentally measure relative changes in capacitance and inductance as a function of stretch in three directions. These experimental relationships are consistent with theoretical predictions that we derive with finite elasticity kinematics.

(Some figures may appear in colour only in the online journal)

1. Introduction

Soft-matter electronics are composed of microchannels of liquid-phase metal alloy, typically eutectic gallium–indium (EGaIn) or gallium–indium–tin (galinstan), embedded in a soft silicone elastomer (e.g. PDMS, Ecoflex® 00-30). In contrast to conventional electronics, these circuits and sensors are elastically soft and can be stretched to several times their natural length without losing electronic functionality. Because they match the elastic compliance of human skin and other natural biological tissue, soft-matter electronics have a potentially central role in emerging domains like biologically-inspired soft robotics and wearable technologies for rehabilitation and human motor assistance. Current applications range from elastically tunable antennae [1, 2] and logic gates [3, 4] to wearable electronic skin [5–10] for monitoring body motion and contact.

Building on these recent efforts, we introduce a new family of soft-matter capacitors and inductors along with theoretical models that accurately predict the relationship between stretch and relative change in capacitance and inductance. All samples are produced by embedding Ecoflex® 00-30 (Smooth-On, Inc.) silicone elastomer with microchannels of galinstan, a metal alloy that is liquid at room temperature (MP $= -19\,^{\circ}$C). We measure their electrical response to tensile and compressive stretch and find that reasonable agreement results with theoretical predictions derived using the kinematics of finite (nonlinear) elasticity.

In addition to hyperelastic strain sensing, we anticipate that soft-matter capacitors and inductors may also be used as circuit elements for wireless communication and analog filtering. These include *RLC* circuits for high frequency band-pass filtering and RF oscillators. Moreover, the proposed theoretical models may be extended to help identify geometries that control the sensitivity and response of the circuit's natural frequency to different modes of elastic deformation.

2. Design overview

We examine the response of the two planar capacitor geometries presented in figures 1(a) and (b). The *square wave* capacitor in figure 1(a) is composed of two serpentine electrodes that share a principal axis. The length of overlap between the two electrodes increases as the capacitor is stretched along this principal direction. For the *spiral*

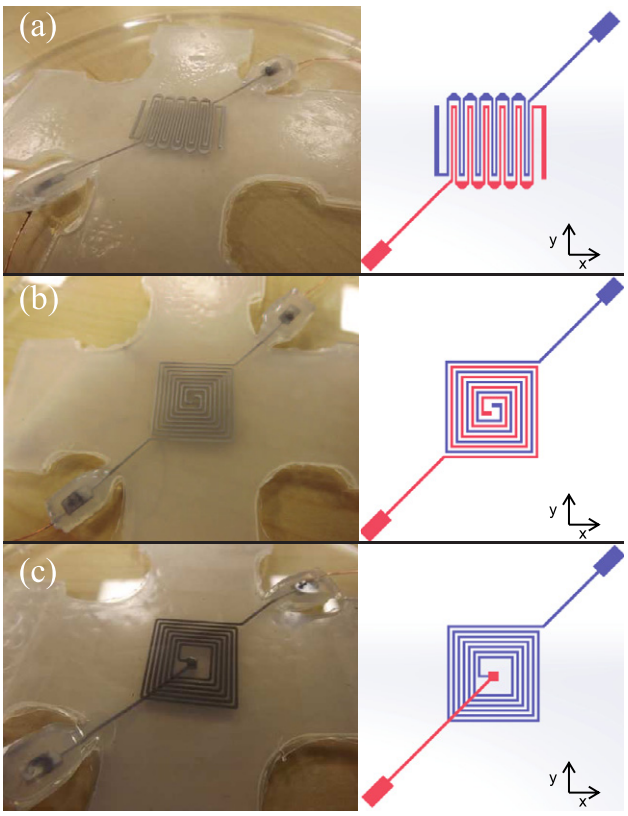

Figure 1. A square wave capacitor (a), a spiral capacitor (b) and a square planar spiral inductor (c). A top down view of channel design is shown on the right. The capacitors are within a single plane; the inductor has a coil in one plane and a bridge that spans over the coil in a separate plane.

capacitor in figure 1(b), the two electrodes wrap around each other to induce a high capacitance per area. As the channels are facing multiple directions, the response to stretch is expected to be more complex.

The capacitive electrodes are long and narrow and so we choose to model them as coplanar parallel strips. The capacitance per length (C') of two equal coplanar strips within a homogeneous medium depends on the width of the strips (s) and half of the width of the gap (g) [11–13],

$$C' = \varepsilon_0 \varepsilon_r \frac{K(k')}{K(k)}. \tag{1}$$

Here, ε_0 and ε_r represent the vacuum permittivity and the relative permittivity, respectively, and $K = K(k)$ is the complete elliptic integral of the first kind. The elliptical integral is calculated for moduli $k = g/(s + g)$ and $k' = \sqrt{1 - k^2}$. This equation assumes infinite thickness of the material above and below the parallel strips and negligible strip thickness. The derivation of (1) can be found in [12, 13]. The total capacitance (C) can be found by multiplying (1) by the length of the electrode (L), such that $C = C'L$.

We are primarily interested in the change in capacitance as a function of the stretches in each Cartesian direction with stretch defined as the ratio of the current dimension to the original dimension (or the strain plus one). We treat the material as elastically homogeneous and assume uniform stretch $\{\lambda_x, \lambda_y, \lambda_z\}$ along the three Cartesian directions. Here, the subscripts x, y, and z correspond to the width, length, and thickness directions of the strips. This implies $L = L_0\lambda_y$, $s = s_0\lambda_x$, and $g = g_0\lambda_x$, where the subscript 0 indicates the initial value (prior to stretching). Under stretch, the capacitance becomes

$$C = \varepsilon_0 \varepsilon_r \frac{K(k_0')}{K(k_0)} L_0 \lambda_y \equiv C_0 \lambda_y \tag{2}$$

and $C/C_0 = \lambda_y$ is the relative change in capacitance (derivation located in the appendix). It is important to note that the capacitance per unit length term remains the same after stretch, with the stretch in the modulus canceling,

$$k = g_0\lambda_x/(s_0\lambda_x + g_0\lambda_x) = g_0/(s_0 + g_0) \equiv k_0, \tag{3}$$

where k_0 is the pre-stretch modulus. Therefore, the new capacitance only depends on the original capacitance and the stretch along the length of the strips. Also, because the elastomer is virtually incompressible, we impose the constraint $\lambda_x\lambda_y\lambda_z = 1$.

The electrodes of the square wave capacitor are all aligned in the (principal) y direction. Therefore, it follows from (2) and incompressibility that

$$\frac{C}{C_0} = \begin{cases} 1/\sqrt{\lambda_x} \\ \lambda_y \\ 1/\sqrt{\lambda_z} \end{cases} \quad \text{(square wave)} \tag{4}$$

for uniaxial stretch in the three directions, assuming that the stretches in the unloaded directions are equal. In the case of a spiral capacitor, electrodes are aligned along both the x and y directions. Therefore, we can treat this as two square wave capacitors in parallel: one with electrodes aligned with the x axis, the other with electrodes aligned with the y axis, each accounting for half of the spiral capacitor's total capacitance,

$$\frac{C}{C_0} = \begin{cases} \lambda_x/2 + 1/2\sqrt{\lambda_x} \\ \lambda_y/2 + 1/2\sqrt{\lambda_y} \\ 1/\sqrt{\lambda_z} \end{cases} \quad \text{(spiral)}. \tag{5}$$

This approximation is based on the assumption that the corners of the spiral behave similarly to coplanar parallel strips while under stretch.

In addition to capacitance, we also examined the response of the planar inductor in figure 1(c). The inductance L of this *square spiral* geometry is estimated using the *modified Wheeler formula* [14], an empirical equation used to assist in the design of planar inductors of (approximately) regular polygons,

$$L = K_1 \mu_0 \frac{n^2 d_{avg}}{1 + K_2 \rho}. \tag{6}$$

Here, K_1 and K_2 are layout dependent coefficients, μ_0 is the magnetic constant, n is the number of turns, d_{avg} is the average diameter, defined as $0.5(d_{out} + d_{in})$, and ρ is the fill ratio, defined as $(d_{out} - d_{in})/(d_{out} + d_{in})$, where d_{out} and d_{in} are the outer and inner diameters of the inductor, respectively.

Under an equibiaxial stretch of $\lambda_x = \lambda_y = \lambda_{xy}$, the diameters are $d_{out} = d_{out_0}\lambda_{xy}$ and $d_{in} = d_{in_0}\lambda_{xy}$. The

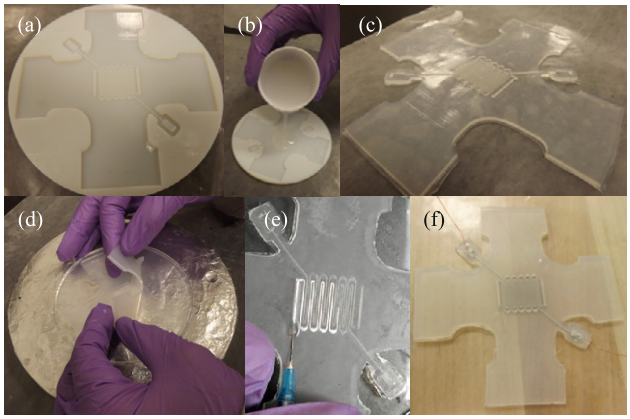

Figure 2. (a) Molds are created in a 3D printer and (b) filled with uncured elastomer. After the elastomer is (c) cured and released, we (d) seal the elastomer and (e) inject the embedded microchannels with galinstan. (f) Copper wires are inserted into the terminals.

inductance then becomes $L = L_0\lambda_{xy}$, where again the subscript 0 denotes the initial values prior to stretch. As with the spiral capacitor, we treat the inductor as being composed of two inductors in series: one with its channels oriented in the x direction and the other with its channels oriented in the y direction, each contributing half the inductance of the device. Again applying the incompressibility constraint, $\lambda_x\lambda_y\lambda_z = 1$, it follows that

$$\frac{L}{L_0} = \begin{cases} \lambda_x/2 + 1/2\sqrt{\lambda_x} \\ \lambda_y/2 + 1/2\sqrt{\lambda_y} \\ 1/\sqrt{\lambda_z}. \end{cases} \tag{7}$$

3. Fabrication and testing

We produce soft-matter capacitors and inductors using the fabrication steps presented in figure 2. Referring to figure 2(a), we use a desktop 3D printer (Objet® 24; Objet, Ltd) to make a plastic (VeroWhitePlus™) mold (that contains a negative of the microchannel features). The channels of the square wave capacitor are 500 μm tall and 400 μm wide with 400 μm wide gaps while the gap and channel widths of the spiral capacitor and square planar spiral inductor are 500 μm. To prepare the mold for casting, we place it in a vacuum oven at -0.9 MPa and 100 °C for an hour in order to remove any solvent in the plastic that might interfere with elastomer curing. Next, we fill the mold with uncured Ecoflex® 00-30 silicone rubber (figure 2(b)), degas and cure the elastomer under vacuum at 100 °C for 1 h, and then remove the cured elastomer from the mold (figure 2(c)).

In order to seal the molded channel features, we prepare a 200 μm thick sealing layer of elastomer and coat the surface with a spin-coated film of additional elastomer that is partially cured on a hotplate at 100 °C for 35 s. Referring to figure 2(d), the two layers of elastomer are bonded by carefully covering the patterned side of the cast elastomer layer with the spin-coated side of the sealing layer. Next, vacuum is applied for several minutes to remove any air bubbles trapped between the two layers. Minimal stresses should be caused at this interface by the bonding process as the elastic modulus of the elastomer is incredibly small (∼125 kPa) [5, 8] and minor deformations will not incur large forces.

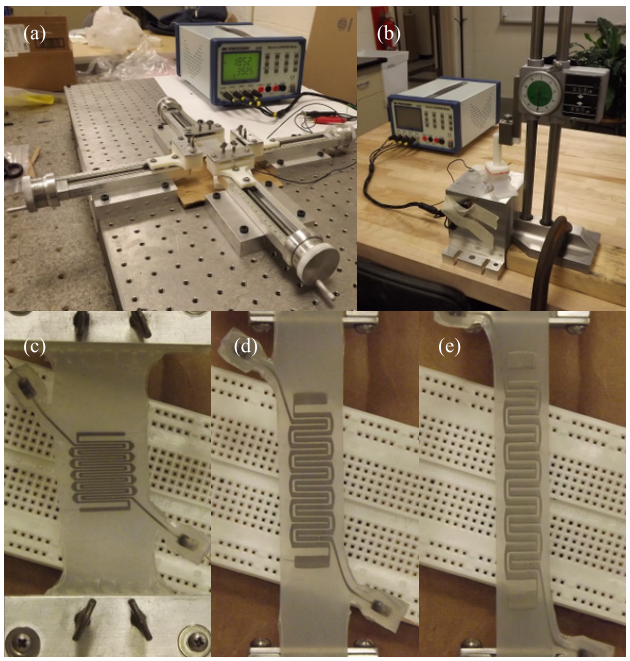

Figure 3. The tensile tests use linear actuators to apply stretch (a). The compression tests use a height gauge to load the sample (b). A BK Precision® 889B Bench LCR/ESR Meter is used in each setup to measure device performance. At the bottom, a square wave sample at λ_x equal to 1 (a), 2 (b) and 3 (c) is shown.

After the two layers are fully bonded, we inject the embedded microchannels with galinstan using a needle and syringe, as shown in figure 2(e). Small drops of Ecoflex® 00-30 are then used to seal any holes or openings created as part of this injection process. To prevent changes in electrical contact resistance, external copper wires are inserted into liquid terminals that are mechanically isolated from the region of elastic deformation (figure 2(f)). Each sample has tabs oriented in both the x and y directions. For uniaxial loading, one set of tabs is removed in order to prevent shape distortion.

The samples are stretched under tension in the x and y directions and compressed in the z direction. Tensile tests are performed using linear actuators and custom made clamps to grip the elastomer tabs (figure 3(a)), and compression tests are performed using a height gauge and compression piece (figure 3(b)). Stretch is applied by incrementally increasing the length (figures 3(c)–(e)). In the tensile tests, the sample is loaded from a stretch of 1 (0% strain) to 3 (200% strain). Under compression, the sample is loaded to a stretch of 0.77 (−23% strain). We also perform cyclic tensile tests for the square wave capacitor along the y direction. For these tests, the stretch is brought to 1.34 (34% strain) and returned to 1 (0% strain) four times, stopping at a stretch of 1.17 in both directions. For all these tests, we use a BK Precision® 889B Bench LCR/ESR Meter to measure capacitance, inductance, and quality factor during loading. These measurements are

performed at 1 V at a frequency of 200 kHz, with the capacitance measured in parallel mode and the inductance measured in series mode.

4. Results

The square wave capacitor samples had an average pre-stretch capacitance of 12.41 pF (and standard deviation of $\sigma = 0.413$, with $n = 7$ individual samples), while the spiral capacitors had a larger output of 17.30 pF ($\sigma = 1.157, n = 5$). The average initial inductance was found to be 0.727 μH ($\sigma = 0.0390, n = 4$) which is close to 0.712 μH (error of 2.2%), the predicted value that can be found using the modified Wheeler formula ($d_{\text{out}} = 19$ mm, $d_{\text{in}} = 7$ mm, $n = 6.5$). It is difficult to predict the capacitance of either of the capacitor designs as the fringing effects from a channel of one electrode to a nonadjacent channel in the other electrode are not accounted for in our theory. The standard deviations are found using the mean of each sample's initial, pre-stretch reading. Experimentally measured values of the normalized change in capacitance and inductance are plotted as a function of stretch in figures 4–8 along with theoretical predictions (shown as a solid black curve), and a fourth-order polynomial fit of the data (shown as a solid gray curve).

The λ_x and λ_y responses for three samples each of the square wave capacitor are presented in figure 4. We observe reasonable agreement between the experimental measurements and the theoretical predictions. When comparing the polynomial fit to the theoretical predictions, we find an error of 6.4% at $\lambda_x = 2$ and 3.2% at $\lambda_x = 3$, and an error of 3.6% at $\lambda_y = 2$ and 11.8% at $\lambda_y = 3$. Nonetheless, for stretch in the x direction, the measured slope appears to be steeper than predicted (figure 4(a)). This may arise from the change in parallel-plate capacitance across the thickness of adjacent channels, a source of capacitance that is not included in our theoretical model. A theoretical prediction based entirely on parallel-plate capacitance ($C/C_0 = 1/\lambda_x^2$) can be seen plotted in figure 4(a) as a dashed line and provides a bound on the experimental measurements. Parallel-plate capacitance is not expected to influence the response to stretch in the y direction and this may explain the stronger agreement in figure 4(b).

It should be noted that there is an apparent increase in variability at very high stretch (>2.8) in figure 4(b). We believe that this originates from a defect in the square wave mold that results in an internal protrusion that pinches the channel closed under high stretch. This closure at some location inside the channel effectively shortens the electrode length and reduces its capacitance. Nonetheless, following this sudden drop in capacitance, additional stretching will lead to the same relative increase in capacitance predicted by the theory. Moreover, the capacitance will return to its previous state if the loading is reduced, implying that the channel has reopened.

Figure 5 shows the λ_x and λ_y responses for four samples of the spiral capacitor, two in each direction. Since the capacitor is orthotropic in the x–y plane, the two response curves appear on the same plot. Again, we see reasonable agreement between the theoretical predictions and

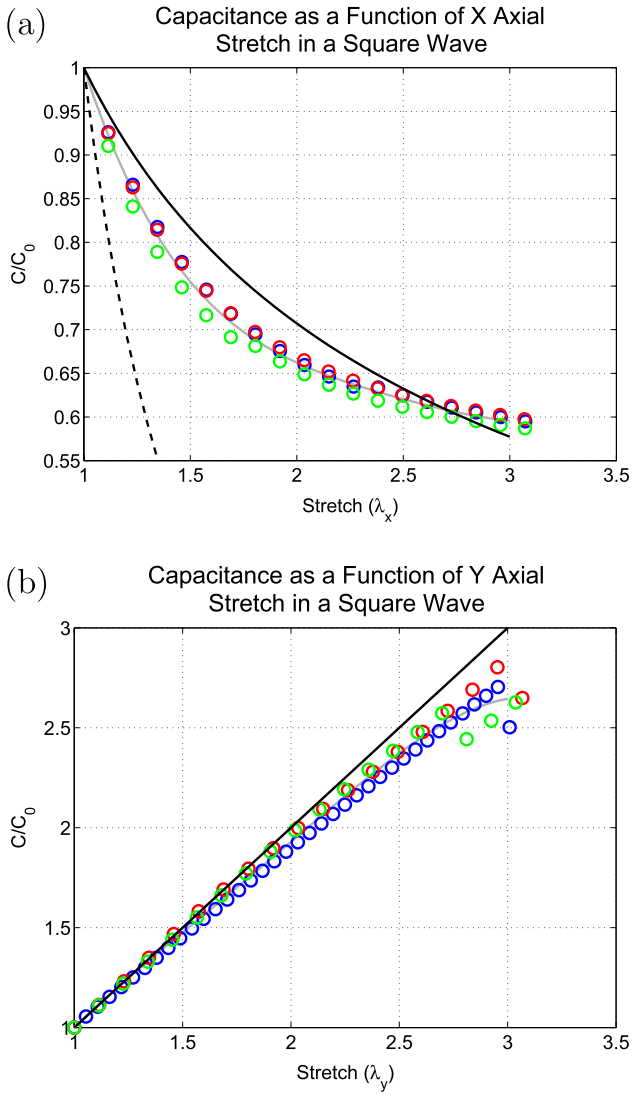

Figure 4. Relative change in capacitance for a square wave capacitor loaded in the (a) x and (b) y directions. The solid black curve represents our theoretical predictions. The solid gray curve represents a fourth-order polynomial fit of the data and is used for statistical analysis. The dashed line in (a) represents a theoretical prediction based upon the assumption that the capacitance is governed by parallel-plate interactions through the thickness of adjacent electrodes.

the experimental results and can find errors of 9.2% and 13.2% at stretches of 2 and 3 using the polynomial fit. However, the theory appears to overestimate the relative change in capacitance. This is likely because the theory does not model the relative change in capacitance at each corner of the spiraling electrodes.

As shown in figure 6, the theory also appears to be consistent with experimental measurements of the inductance as a function of stretch in the x and y directions. Again, because of the orthotropic geometry, the two stretch responses are plotted on the same graph and we performed experiments on two samples for each direction. In contrast to the spiral capacitor, the theoretical predictions appear to underestimate the electrical response, with an error of 11.5% at $\lambda = 2$ and 15.1% at $\lambda = 3$. This may arise from simplifying assumptions

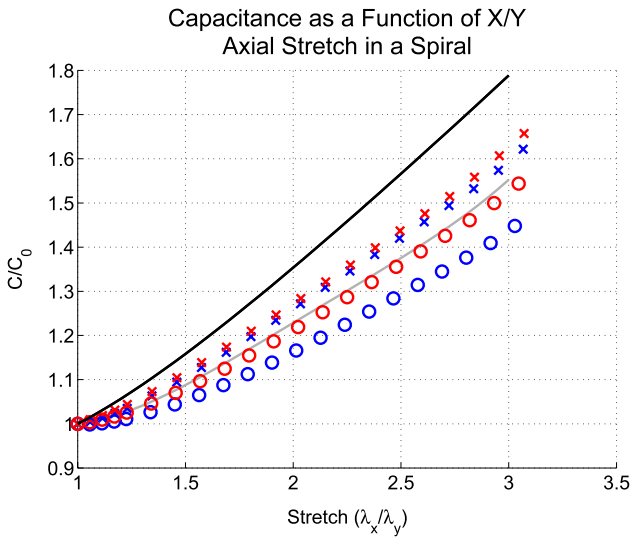

Figure 5. Relative change in capacitance for a spiral capacitor loaded in the x ($\times$) and y ($\circ$) directions.

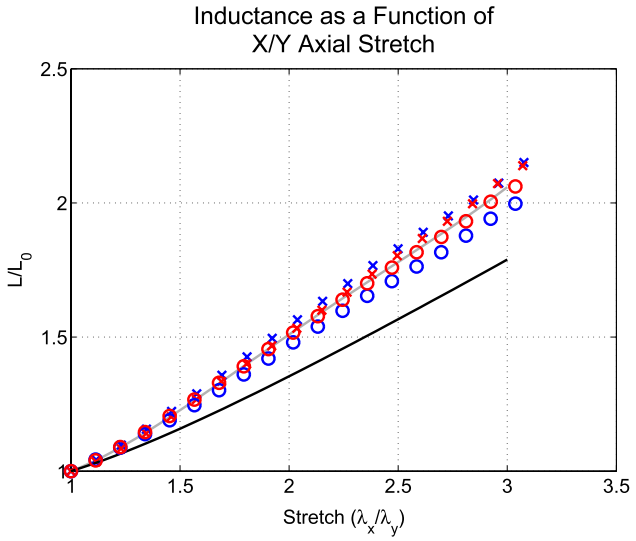

Figure 6. Relative change in inductance for a spiral inductor loaded in the x ($\times$) and y ($\circ$) directions.

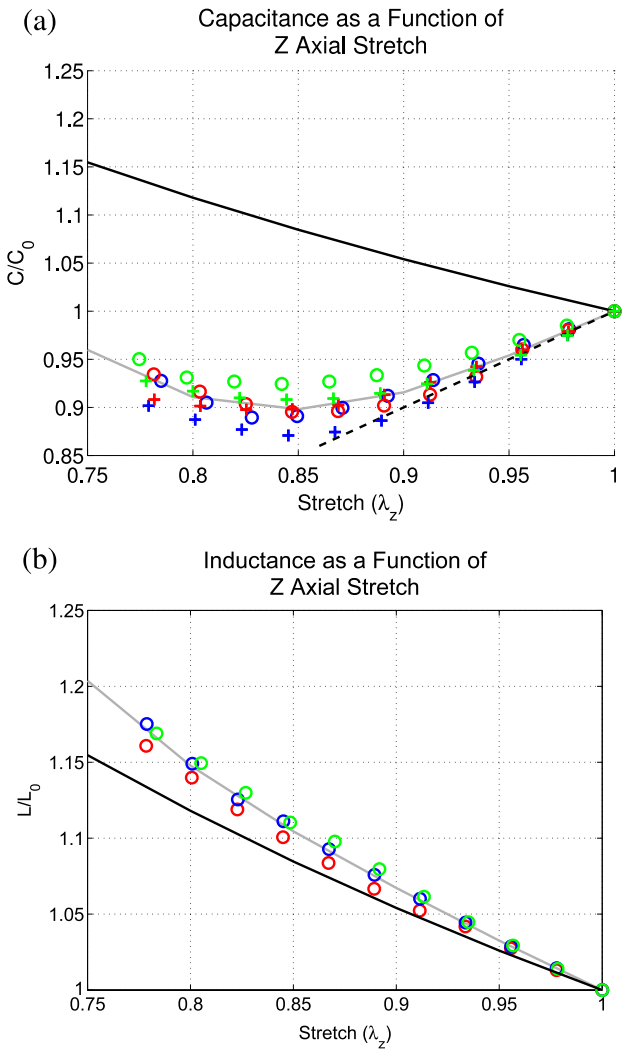

Figure 7. Relative change in (a) capacitance and (b) inductance for compression in the z direction. The dashed curve in (a) represents the theoretical prediction based on the assumption that the capacitance is governed by the parallel-plate interaction through the thickness of adjacent electrodes. Both the square wave ($\circ$) and spiral ($+$) capacitor designs are plotted in (a).

in the modified Wheeler formula as well as the distortion of the inductor from its initially square spiral shape.

Figures 7(a) and (b) present the response of the capacitors and inductors to compression in the z direction, respectively. Referring to figure 7(a), the theory clearly fails to capture the non-monotonic dependence of the capacitance on the transverse compression, having a per cent error of 17.7% when $\lambda_z = 0.8$. For lighter compressive loads, the capacitance appears to decrease even though the parallel strips are widening. This suggests that the electrical response may be governed by the parallel-plate capacitance through the electrode thickness, which decreases under compression. In this case, we expect $C/C_0 = \lambda_z$ (dashed line in figure 7(a)), which appears to agree with the experimental results for $0.9 \geq \lambda_z \geq 1$. For higher loads ($\lambda_z < 0.85$), the electrodes flatten out and the relative change in capacitance appears to have a slope that is consistent with the theoretical predictions from the parallel strip model. In contrast, the theory appears to be in reasonable agreement with the experimental response of the inductor over the complete range of compressive stretches ($0.75 \geq \lambda_z \geq 1$), having a per cent error of only 2.7% at a stretch of 0.8.

The results from the cyclic loading tests, presented in figures 8(a) and (b), show strong repeatability and low hysteresis. The standard deviation of the normalized capacitance for each point in the cycle was found to be less than 0.002 for each of the two samples. Referring to figure 8(b), we did not measure statistically significant differences in the capacitance for $\lambda_y = 1.17$ when comparing values during loading and unloading over repeated cycles.

Lastly, we measured the quality factor of the inductor for stretch in all three Cartesian directions. This factor can be defined as the ratio of the capacitive reactance $1/\omega C$ or inductive reactance ωL to the parasitic resistance of

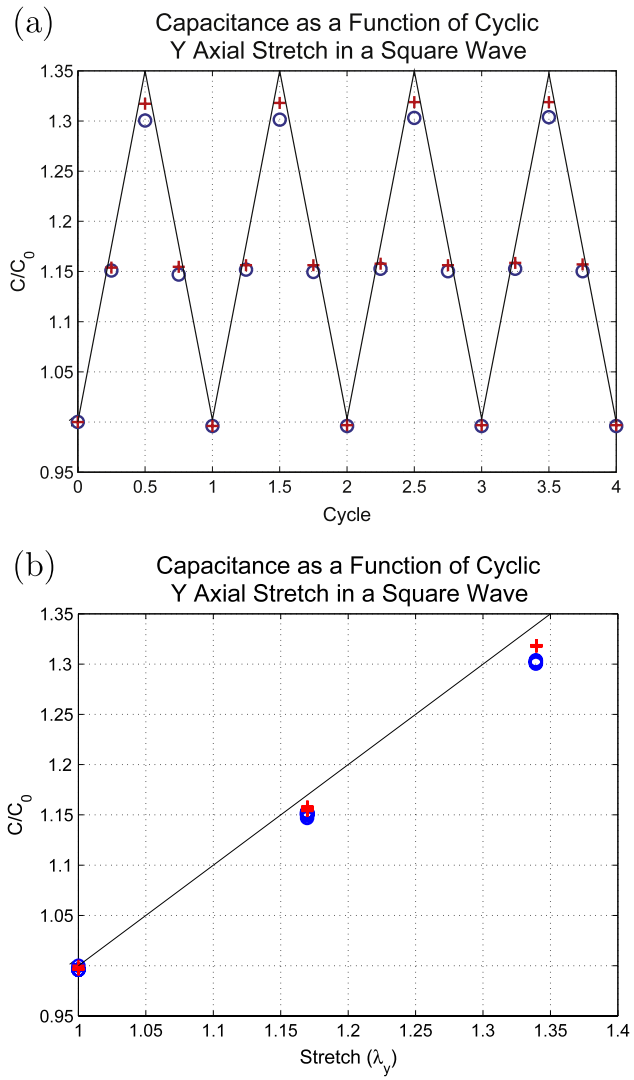

Figure 8. Cyclical response versus (a) cycle number and (b) stretch of a square wave capacitor for stretch in the y direction for two samples (denoted by '$\circ$' and '$+$' markers).

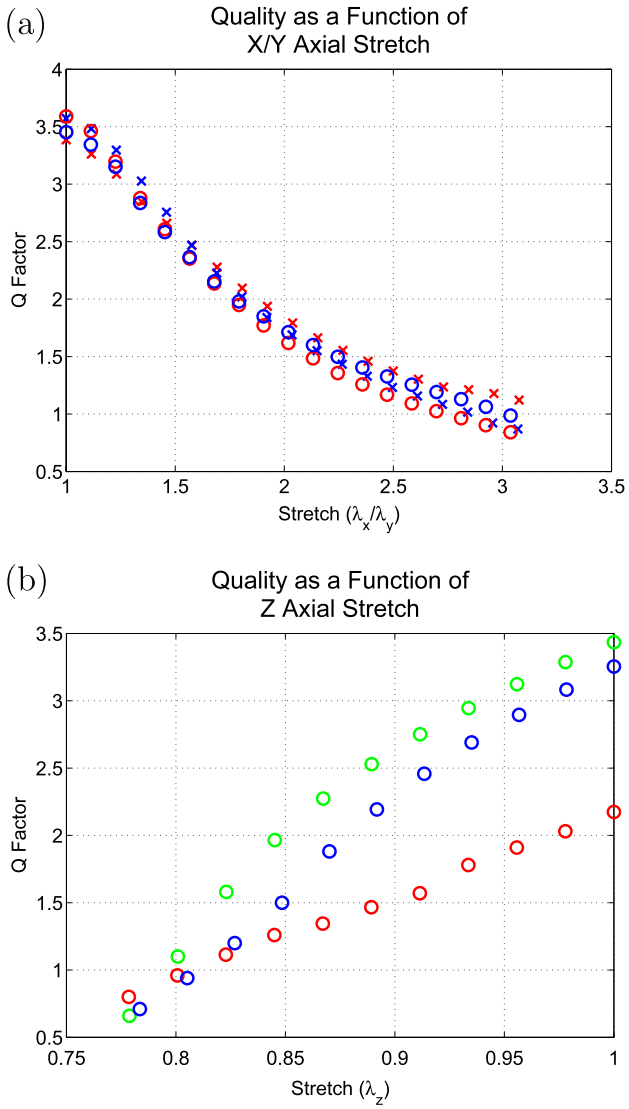

Figure 9. The quality factor of the inductor measurements under loading in the (a) x/y and (b) z directions.

the device, where ω is the angular electrical frequency. As shown in figure 9(a), the quality factor decreases with increasing tensile stretch. Under compression, the quality factor decreases with decreasing stretch (i.e. increasing compression), reaching a value of less than 1 when $\lambda_z < 0.8$. The quality factor of the capacitors was too high to measure accurately with our *LCR* meter at all values of stretch. This suggests that the current leakage is extremely low for the testing frequencies of interest.

5. Discussion

The soft-matter capacitors and inductor presented in figure 1 remain electrically functional when elongated to three times their natural length. Because they are intrinsically soft and elastic, these circuit elements match the compliance of natural biological tissue and can potentially be incorporated in wearable technologies and so-called 'artificial skin' for biologically-inspired soft robots. The capacitors and inductor are composed of silicone elastomer (Ecoflex® 00-30) embedded with microchannels of liquid-phase metal alloy (galinstan). As demonstrated in figure 2, we produce the microchannel features by replica casting the elastomer in a 3D printed mold. After bonding a sealing layer of elastomer, we inject the embedded microchannels with liquid alloy using a needle and syringe.

As with other soft-matter circuits, the capacitors and inductor respond electrically to elastic deformation. To characterize this response, we performed a series of tensile and compressive tests in the planar x/y and transverse z directions. Both the experimental measurements and theoretical predictions are presented in figures 4–7. As expected, the relative changes in capacitance and inductance change monotonically with stretch. The only exception was the response of the capacitors under compressive loading in the z direction, where we measured a relative decrease in capacitance under light load followed by increased capacitance under increasing load.

The square wave capacitor (figure 1(a)) responds linearly when stretched along the length of its electrodes (figure 4(b)). The cyclic loading tests (figure 8) demonstrate strong repeatability and no hysteresis for low and moderate stretches. Together, these factors suggest that square wave capacitors could be used as an alternative to moiré interferometry [15] for measuring the strain of unreinforced plastics, nylon, elastomers, and other soft materials that significantly alter the gauge factor of conventional wire and foil strain gauges [16, 17]. Moreover, they could potentially be incorporated into piezoelectric [18], ionic-polymer–metal [19], and other composite actuators in order to monitor deformation without altering the actuator's mechanical properties. The strain sensing resolution ($\Delta\varepsilon$) of this design is dependent on the resolution of the capacitive sensor (ΔC) such that $\Delta\varepsilon = \Delta C/C_0$ (derivation can be found in the appendix). Further analysis of the linearity and any temperature dependence would be required before application of this design to a strain gauge.

With the exception of the capacitors under transverse compression, the theoretical predictions appear to be in reasonable agreement with the experimental results. This is accomplished without the aid of any data fitting. According to equations (4), (5), and (7), the mappings between stretch and the relative change in capacitance or inductance do not depend on the original values of the channel length, height, width, or spacing. However, these system parameters may be required to obtain more accurate theoretical predictions that account for influences from parallel-plate capacitance, edge-effects from the electrode corners, shape distortion, and the thickness of the dielectric material. Parallel-plate capacitance is particularly important in predicting the response of the capacitors to transverse compression. This may in part be due to the channels collapsing under compression, causing the effective λ_z of the channel to be smaller than the λ_z applied on the sample. Referring to figure 7(a), the theoretical dashed line obtained by assuming that the capacitance is governed by the parallel-plate interactions through the thickness of the electrodes appears to be in much stronger agreement with the experimental measurements compared to the prediction based on the width-controlled interaction of thin parallel strips. While more accurate predictions can also be obtained with finite element modeling, the present analytic techniques yield closed-form algebraic relationships that can be very helpful in informing design.

Alternatively, it may be possible to improve the accuracy of our theoretical predictions through changes in fabrication and design of samples, particularly of the channel cross section. A reduction in the channel height would reduce the parallel-plate capacitance. Thus, the total capacitance of a sample would be more dependent on coplanar parallel strip capacitance, which is the basis of our theoretical model. The limiting factor in controlling the height is the bonding step, during which the partially cured elastomer on the spun coat layer may adhere to the top of the channel, closing it and preventing injection.

Independent measurement of stretch in the three Cartesian directions requires three sensors with different orientations. This can be achieved because, according to our theory, the capacitance of a square wave capacitor changes only as a function of the stretch along the electrodes. The capacitance change incurred by cross axial stretches is a result of the near incompressibility of the elastomer, which leads to mechanical coupling between transverse deformation and changes in the electrode length and a corresponding change in capacitance. This allows for three electrical response measurements that may be inverted to establish the three values of stretch $\{\lambda_x, \lambda_y, \lambda_z\}$. Additional testing would be required to ensure that complex loading does not cause electrical responses that are not predicted by our uniaxial theories, as well as to reexamine the effects of z axial stretch (relative to the capacitor) to develop more accurate equations. Regardless, bidirectional stretch measurement $\{\lambda_x, \lambda_y\}$ can be achieved using two orthogonally oriented planar sensors.

While the relative increase in the capacitance of the square wave capacitor is linearly proportional to stretch, the spiral capacitor is relatively insensitive, with relative capacitive increasing by a factor of approximately 1.1 under a stretch of 1.5. Because of this, spiral capacitors would be ineffective as strain sensors, but may be useful in applications where minimal response to stretch is desired, such as wearable electronics. Future efforts may focus on modifications to the spiral geometry to completely eliminate electrical response to planar stretch, making its performance insensitive to any deformations. This may require a combination of capacitive elements in series or parallel to compensate for any stretch response.

6. Conclusion

By extending existing principles in soft-matter electronics, we introduce a new family of inductors and capacitors that are soft and highly stretchable. These circuit elements respond to tensile stretch in the planar x and y directions and compression in the transverse z direction. In general, we find good agreement between the experimental measurements and theoretical predictions based on finite elasticity kinematics. Moreover, the square wave capacitor exhibits strong repeatability and a linear electrical response to stretch, properties that are ideal for most strain sensing applications.

We plan to eventually combine these capacitors and inductors to produce soft-matter *LC* and *RLC* circuits for frequency band-pass filtering and stretchable RF devices. Potential applications include wireless strain sensing and frequency-controlled registration of sensors in a large array. While the inductors have adequate inductance (of the order of μH), the capacitors will need to be redesigned in order to increase the capacitance from the current pF values. These soft-matter electronics could be placed on the skin and around joints without interfering with the body's natural compliance and motion. Applications in wearable electronics may require careful pairing of soft-matter capacitor and inductor elements that minimize electrical response to elastic deformation. Such pairings will be informed by the coupling laws presented here along with new theoretical insights obtained by future improvements to our models.

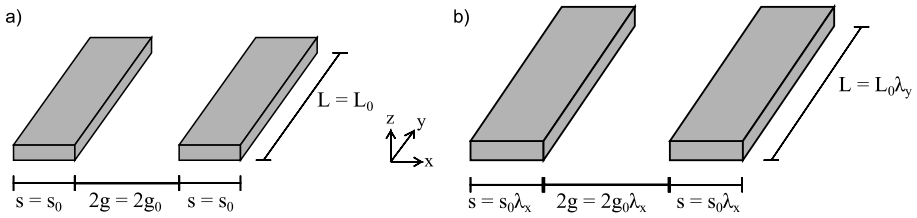

Figure A.1. Coplanar parallel strips before (a) and after (b) a stretch field $\{\lambda_x, \lambda_y, \lambda_z\}$ is applied to the system.

Appendix. Derivation of capacitive theory and sensing resolution

The capacitive theories we developed are derived from (1), which is used to calculate the capacitance per length of the coplanar strips illustrated in figure A.1 [12, 13]. This prediction assumes that the strips have negligible thickness and are embedded in an infinite dielectric medium with a fixed dielectric constant. Multiplying (1) by the length of the coplanar strip (L) then yields

$$C = \varepsilon_0 \varepsilon_r \frac{K(k')}{K(k)} L$$

with $k = g/(s+g)$ and $k' = \sqrt{1-k^2}$ as before.

If we now define the initial, pre-stretch, geometry as L_0, s_0, and g_0 (figure A.1(a)), as well as define the initial modulus $k_0 = g_0/(s_0+g_0)$, it can be found that the pre-stretch capacitance (C_0) is

$$C_0 = \varepsilon_0 \varepsilon_r \frac{K(k_0')}{K(k_0)} L_0.$$

We are primarily interested in the case when deformations occur, so we will apply a uniform stretch in each of the Cartesian directions $\{\lambda_x, \lambda_y, \lambda_z\}$, where $x = x_0\lambda_x$ and x_0 is the initial pre-stretch value. This affects the current geometry of the coplanar strips, causing $g = g_0\lambda_x$, $s = s_0\lambda_x$, and $L = L_0\lambda_y$, as seen in figure A.1(b). The current modulus is then $k = g_0\lambda_x/(s_0\lambda_x + g_0\lambda_x)$, which is equivalent to the pre-stretch modulus k_0 since the λ_x values in the numerator and denominator cancel out. This then results in (2),

$$C = \varepsilon_0 \varepsilon_r \frac{K(k_0')}{K(k_0)} L_0 \lambda_y \equiv C_0 \lambda_y.$$

Lastly, the strain measurement resolution ($\Delta\varepsilon$) corresponds to the smallest measurable difference in capacitance (ΔC). This value is obtained by replacing the stretch λ with the expression $\lambda = 1 + \varepsilon$, which relates stretch with strain ε, and then taking the derivative of (2). This leads to the following result for the strain resolution:

$$\Delta\varepsilon = \Delta C / C_0.$$

References

[1] So J H, Thelen J, Qusba A, Hayes G J, Lazzi G and Dickey M D 2009 Reversibly deformable and mechanically tunable fluidic antennas *Adv. Funct. Mater.* **19** 3632–7

[2] Cheng S and Wu Z 2011 A microfluidic, reversibly stretchable, large-area wireless strain sensor *Adv. Funct. Mater.* **21** 2282–90

[3] So J H, Koo H J, Dickey M D and Velev O D 2012 Ionic current rectification in soft-matter diodes with liquid–metal electrodes *Adv. Funct. Mater.* **22** 625–31

[4] Koo H J, So J H, Dickey M D and Velev O D 2011 Towards all-soft matter circuits: prototypes of quasi-liquid devices with memristor characteristics *Adv. Mater.* **23** 3559–64

[5] Park Y L, Majidi C, Kramer R, Bérard P and Wood R J 2012 Hyperelastic pressure sensing with a liquid-embedded elastomer *J. Micromech. Microeng.* **20** 125029

[6] Majidi C, Kramer R and Wood R J 2011 A non-differential elastomer curvature sensor for softer-than-skin electronics *Smart Mater. Struct.* **20** 105017

[7] Kramer R K, Majidi C and Wood R J 2011 Wearable tactile keypad with stretchable artificial skin *IEEE Int. Conf. on Robotics and Automation (Shanghai)* pp 1103–7

[8] Kramer R K, Majidi C, Sahai R and Wood R J 2011 Soft curvature sensors for joint angle proprioception *IEEE Int. Conf. on Intelligent Robots and Systems (San Francisco)* pp 1919–26

[9] Park Y L, Chen B and Wood R J 2012 Design and fabrication of soft artificial skin using embedded microchannels and liquid conductors *IEEE Sensors J.* **12** 2711–8

[10] Wong R D P, Posner J D and Santos V J 2012 Flexible microfluidic normal force sensor skin for tactile feedback *Sensors Actuators* A **179** 62–9

[11] Gevorgian S and Berg H 2001 Line capacitance and impedance of coplanar-strip waveguides on substrates with multiple dielectric layers *European Microwave Conf. (London)* vol 2, pp 5–8

[12] Gevorgian S, Berg H, Jacobsson H and Lewin T 2003 Application notes-basic parameters of coplanar-strip waveguides on multilayer dielectric/semiconductor substrates, part 1: high permittivity superstrates *IEEE Microw. Mag.* **4** 60–70

[13] Di Paolo F 2000 *Networks and Devices Using Planar Transmissions Lines* (New York: CRC Press) pp 347–349, pp 378–81

[14] Mohan S S, del Mar Hershenson M, Boyd S P and Lee T H 1999 Simple accurate expressions for planar spiral inductances *IEEE J. Solid-State Circuits* **34** 1419–24

[15] Chiang F-P 1979 Moiré methods of strain analysis *Exp. Mech.* **19** 290–308

[16] Stehlin P 1972 Strain distribution in and around strain gauges *J. Strain Anal. Eng. Des.* **7** 228–35

[17] Beatty M and Chewning S 1979 Numerical analysis of the reinforcement effect of a strain gage applied to a soft material *Int. J. Eng. Sci.* **17** 907–15

[18] Crawley E F and Anderson E H 1990 Detailed models of piezoceramic actuation of beams *J. Intell. Mater. Syst. Struct.* **1** 4–25

[19] Shahinpoor M, Bar-Cohen Y, Simpson J O and Smith J 1998 Ionic polymer–metal composites (IPMCs) as biomimetic sensors, actuators and artificial muscles—a review *Smart Mater. Struct.* **7** R15